ScieRxiv
NOT PEER-REVIEWED
Research Article

Frequency-thickness normalized electromagnetic parameter design for broadband electromagnetic wave absorption in FeCoCu alloy foams

Bo Hu, Yanyi Chen, Weikang Song, Yongzheng Chen, Xuan Wang, Xijiang Han*, and Yunchen Du*

State Key Laboratory of Space Power-Sources, School of Chemistry and Chemical Engineering, Harbin Institute of Technology, Harbin 150001, Heilongjiang, China.

***Correspondence to:** Prof. Yunchen Du and Prof. Xijiang Han, State Key Laboratory of Space Power-Sources, School of Chemistry and Chemical Engineering, Harbin Institute of Technology, Harbin 150001, Heilongjiang, China. E-mail: yunchendu@hit.edu.cn; hanxijiang@hit.edu.cn.

Received: 24 May 2026 | Approved: 01 June 2026 | Online: 01 June 2026

Abstract

Electromagnetic wave absorbing materials (EWAMs) are critical for mitigating electromagnetic (EM) pollution, yet achieving broadband absorption with thin coatings remains challenging because clear criteria for EM parameters optimization are still lacking. Herein, a frequency-thickness normalized EM parameters construction strategy is proposed based on transmission line theory. By quantitatively correlating complex permittivity, frequency, and coating thickness with reflection-loss minimization, the optimal complex permittivity for thin broadband absorption is constructed as $\varepsilon_r'=\left(\frac{76}{fd}\right)^2$, and $\varepsilon_r''=\frac{95}{fd}$ (f in GHz and d in mm), thereby identifying the target complex permittivity distribution. The results show that pure conduction loss inherently deviates from the required parameter evolution and limits effective absorption bandwidths (EABs), whereas polarization and magnetic losses provide additional tunable degrees of freedom

to approach optimal absorption conditions. To validate this theory-guided design principle, FeCoCu alloy foams with tunable Cu contents were synthesized. Cu incorporation regulates conduction loss and induces BCC/FCC dual phases, generating abundant heterogeneous interfaces for interfacial polarization, while the FeCo matrix preserves desirable magnetic loss. An equivalent circuit model further elucidates the dielectric loss mechanism, revealing that Cu mainly enhances interfacial polarization intensity rather than changing relaxation dynamics. Benefiting from the optimized coupling of conduction loss, polarization loss, magnetic loss, impedance matching, and quarter-wavelength cancellation, the $Fe_{65}Co_{30}Cu_5$ foam achieves an effective absorption bandwidth of 7.36 GHz with a coating thickness of 1.74 mm. This work provides a theory-guided framework for constructing optimal EM parameters and understanding dielectric loss mechanisms toward thin, efficient, and broadband EWAMs.

Keywords: Electromagnetic wave absorption, permittivity-frequency-thickness relationship, metallic alloy foam, broadband absorption, transmission line theory

INTRODUCTION

The rapid proliferation of electronic devices and wireless communication systems has led to an increasingly complex electromagnetic (EM) environment, raising growing concerns regarding EM pollution[1-3]. EM wave absorbing materials (EWAMs) are therefore widely regarded as an effective solution for suppressing unwanted EM radiation and ensuring the reliable operation of electronic systems[4,5]. Ideal EWAMs are generally expected to exhibit strong EM absorption intensity, broad effective absorption bandwidth (EAB) with thin coating thickness to meet the demands of device miniaturization and integration[6,7]. A wide variety of material systems, including carbon-based materials, magnetic metals, ceramics, and their composites, have been reported as promising EWAMs with broadband absorption. However, despite decades of intensive research, achieving broadband EM wave absorption with thin coatings remains a fundamental and unresolved challenge.

With a given coating thickness, achieving effective EM absorption requires the EM parameters of EWAMs to satisfy a specific relationship at different frequencies, which imposes an intrinsic constraint on broadband EM absorption with thin coating thicknesses. From a mechanistic perspective, EM wave absorption can be commonly

attributed to conduction loss, polarization loss, and magnetic loss[8,9]. Many studies have demonstrated that introducing multiple EM loss mechanisms can effectively broaden the EAB[10,11]. Accordingly, numerous strategies have been proposed to enhance one or more of these loss mechanisms, such as increasing electrical conductivity, constructing heterogeneous interfaces, introducing dipolar defects, or incorporating magnetic components[12,13]. For instance, Liu *et al.* ingeniously fabricated ZnO/NiO/N-doped carbon/CNT composites through microwave non-equilibrium pyrolysis of Zn-Ni bimetallic MOF/CNT precursors. The CNT scaffold with strong microwave-coupling capability induces plasma arc discharge and transient thermal shock, promoting the confined nucleation and nanoscale dispersion of ZnO/NiO within the carbon matrix. The abundant ZnO/NiO/carbon heterointerfaces generate pronounced interfacial polarization, while N-doped carbon and CNTs contribute dipolar polarization and moderate conduction loss. Benefiting from these synergistic dielectric loss mechanisms and improved impedance matching, the optimized BMO-carbon/CNT-2 composite achieves a minimum reflection loss of -55.16 dB at 1.85 mm and an EAB of 4.64 GHz[14]. However, merely increasing the number of loss mechanisms through compositional regulation and microstructural design does not necessarily lead to a further expansion of EAB. This is because the reflection loss (RL) values of an EWAM are determined by both the impedance matching characteristics at the air-EWAM interface and the intrinsic EM attenuation capability within the EWAM[15-17]. Effective impedance matching requires the magnetic loss capacity to be comparable to dielectric loss. However, in dielectric-loss-dominated systems, the magnetic loss introduced by incorporating magnetic components is often negligible[18,19]. Consequently, satisfactory impedance matching can only be achieved within a relatively narrow frequency range.

The EAB and coating thickness of EWAMs are fundamentally constrained by the Planck-Rozanov limit ($\frac{\Delta\lambda}{d}<\frac{16\mu_s}{\rho_0}$), which establishes an intrinsic trade-off between these parameters. According to this constraint, a higher magnetic permeability generally enables a broader achievable EAB, highlighting the importance of developing EWAMs with enhanced magnetic response. Some researchers employ pristine magnetic metals as EWAMs and have achieved promising results[20,21]. Although magnetic metals intrinsically possess high electrical conductivity and saturation magnetization, they are typically incorporated into practical EWAMs in the form of micro-/nanoparticles

dispersed within insulating matrices (e.g., resin or paraffin). As a result, continuous conductive networks are difficult to establish, and the macroscopic conduction loss as well as dielectric loss contribution of the composites is often limited. Meanwhile, the magnetic loss capability of magnetic metals in the GHz range is significantly constrained by the Snoek's limit, leading to a rapid attenuation of magnetic response at higher frequencies[22-24]. Enhancing dielectric loss within a ferromagnetic matrix has been considered an effective strategy to compensate for insufficient high-frequency magnetic attenuation. For example, Qiu's group developed $FeCoNiCuC_{0.37}$ high-entropy alloys through lattice distortion engineering. The pronounced lattice distortion induced by C incorporation decreases electrical conductivity and generates abundant dipolar polarization centers, thereby alleviating impedance mismatch and enhancing polarization loss. Benefiting from the optimized impedance matching and boosted dipolar polarization, the $FeCoNiCuC_{0.37}$ alloy delivers remarkable EM wave absorption performance, achieving a minimum reflection loss of -65.4 dB and an EAB of 6.81 GHz[25]. Nevertheless, the intrinsically high electrical conductivity of HEA systems may still cause impedance mismatch, highlighting the importance of rational dielectric regulation for further bandwidth expansion. More importantly, the optimization of EM absorption performance in most reported EWAMs remains largely empirical, and a unified physical criterion that correlates EM parameters, coating thickness, and operating frequency is still lacking. Consequently, the rational design of thin EWAMs with broadband performance remains challenging.

Based on the above considerations, transmission line theory was firstly employed to establish the functional relationship among relative permittivity, coating thickness, and frequency required for achieving optimal EM absorption. It's also demonstrated that single conduction loss mechanism is insufficient to realize broadband absorption, whereas the incorporation of additional polarization and magnetic loss mechanisms can effectively relax this constraint and broaden the achievable bandwidth. Inspired by these findings, FeCo foams are initially fabricated via an auto-combustion process followed by H_2 reduction, and different amounts of Cu were subsequently introduced. The incorporation of Cu not only enables regulation of conduction loss but also promotes interfacial polarization due to the coexistence of BCC and FCC crystalline phases. Benefiting from the strong magnetic loss capability of the FeCo alloy, the enhanced conductive and interfacial polarization losses induced by Cu addition, and the formation

of conductive networks facilitated by the foam-like architecture, the composition-optimized FeCoCu foam ($Fe_{65}Co_{30}Cu_5$ foam) exhibits pronounced broadband EM absorption performance. Notably, an EAB of 7.36 GHz is achieved with coating thickness only 1.74 mm. This work not only demonstrates a broadband EWAMs but also establishes a physically grounded design framework for the rational development of thin, broadband EWAMs.

EXPERIMENTAL

Synthesis of FeCo foam and FeCoCu foam

FeCo alloy foam was fabricated through a sol-gel auto-combustion process followed by hydrogen reduction. Briefly, 3.030 g (7.5 mmol) of $Fe(NO_3)_3 \cdot 9H_2O$, 0.728 g (2.5 mmol) of $Co(NO_3)_2 \cdot 6H_2O$, and 1.239 g (16.5 mmol) of glycine were dissolved in 100 mL of deionized water under continuous magnetic stirring for 30 min to obtain a homogeneous precursor solution. The solution was subsequently heated to 220 °C to remove excess water, during which self-sustained combustion was triggered. The resulting oxide precursor was then reduced at 550 °C for 6 h in a 5% H_2/95% Ar atmosphere with a heating rate of 3 °C/min, yielding the FeCo alloy foam.

FeCoCu alloy foams with varying Cu contents were prepared using an identical synthetic protocol. Specifically, 5 at.%, 10 at.%, and 20 at.% of Fe were substituted by Cu in the precursor formulation. The obtained samples were designated as $Fe_{65}Co_{30}Cu_5$ foam, $Fe_{60}Co_{30}Cu_{10}$ foam, and $Fe_{50}Co_{30}Cu_{20}$ foam, respectively.

Characterization

SEM images were collected using a Regulus 8230 scanning electron microscope. TEM observations were performed on a Tecnai F20 transmission electron microscope. Powder X-ray diffraction (XRD) patterns were recorded on a Rigaku D/MAXRC diffractometer equipped with Cu Kα radiation operated at 40.0 kV and 40.0 mA. Magnetic hysteresis loops were measured using a vibrating sample magnetometer (VSM, LakeShore, Model 7404 series). Inductively coupled plasma atomic emission spectroscopy (ICP-AES) was carried out using an Optima 8300 instrument (PerkinElmer, USA). For electromagnetic parameter measurements, the as-prepared products were mixed with paraffin at a mass ratio of 60:40 and pressed into toroidal specimens with a thickness of 2.00 mm, an outer diameter of 7.00 mm, and an inner

diameter of 3.04 mm. The complex permittivity and permeability were measured using an Agilent N5234A vector network analyzer (Agilent, USA).

Theoretical calculation and CST simulation

To establish the quantitative relationship between EM parameters, thickness, and frequency for optimal absorption, the reflection loss (RL) was calculated based on classical transmission line theory. The RL values are expressed as[26-29]:

$$RL(dB)=20\log_{f_0}\left(\frac{Z_{in}-1}{Z_{in}+1}\right) \quad (1)$$

$$Z_{in}=\sqrt{\frac{\mu_r}{\varepsilon_r}}\tanh\left(\frac{j2\pi fd\sqrt{\mu_r\varepsilon_r}}{c}\right) \quad (2)$$

where Z_{in} is the normalized input impedance, c is the velocity of EM wave in vacuum, and d is the coating thickness of EWAMs. The frequency was varied from 6.00 to 18.00 GHz (step: 0.01 GHz), and the thickness ranged from 1.00 to 3.00 mm (step: 0.25 mm). For each fixed combination of f and d, μ_r was set to 1.00-0.00j to isolate dielectric contributions. The real (ε_r') and imaginary (ε_r'') parts of permittivity were systematically scanned within 0.00-200.00 (step: 0.10), and the corresponding values yielding the minimum RL were extracted.

To evaluate the intrinsic bandwidth limitation of pure conduction loss, the free electron model was adopted. In this case, ε_r' was treated as a frequency-independent constant ($\varepsilon_r' = k$), which represents the real permittivity in the conduction-loss model, while ε_r'' follows[30, 31]:

$$\varepsilon_r''=\frac{\sigma}{2\pi f\varepsilon_0} \quad (3)$$

where σ is the electrical conductivity and ε_0 is the vacuum permittivity. The parameter k was varied from 3.00 to 18.00 (step: 3.00), and σ ranged from 0.00 to 6.00 S/m (step: 0.01 S/m.

For polarization-dominated loss, the Debye relaxation model was employed to

determine the maximum achievable bandwidth under a single relaxation process[32, 33]:

$$\varepsilon_r'=\varepsilon_\infty+\frac{\varepsilon_s-\varepsilon_\infty}{1+(2\pi f\tau)^2} \quad (4)$$

$$\varepsilon_r''=\frac{(\varepsilon_s-\varepsilon_\infty)2\pi f\tau}{1+(2\pi f\tau)^2} \quad (5)$$

where σ, ε_∞, ε_s and τ refers to the electrical conductivity, the dielectric permittivity at high-frequency limit, the static permittivity and the relaxation time, respectively. The parameter ε_∞ was varied from 0.00 to 10.00 (step: 0.10), ε_s-ε_∞ ranged from 0.00 to 20.00 (step: 0.10), and $1/\tau$ was scanned within 5.0×10^{10} s^{-1} -20.0×10^{10} s^{-1}(step: 1.0×10^{9} s^{-1}).

All EM simulations were conducted using CST Microwave Studio 2019. For radar cross-section (RCS) simulations, a square PEC plate (thickness: 1.0 mm, side length: 180 mm) was coated with a 1.75 mm EM absorbing layer ($Fe_{70}Co_{30}$, $Fe_{65}Co_{30}Cu_5$, $Fe_{60}Co_{30}Cu_{10}$, and $Fe_{50}Co_{30}Cu_{20}$ foam, respectively). The simulation frequency ranged from 2.00 to 18.00 GHz (step: 0.08 GHz). Open boundary conditions were applied in all directions, and a plane wave was incident along the -*z* direction. For angular-dependent RCS evaluation, the frequency was fixed at 9.20 GHz, and the incident angle was scanned from -90° to 90° (step: 1°), with other parameters unchanged. The EM absorption performance of the multilayer periodic structure was simulated under similar conditions, except that a waveguide port excitation (Port 1 along -*z*) was used. The structure consisted of a PEC backing layer (1.0 mm) and four EM absorbing layers (each 1.5 mm thick), with lateral dimensions of 6.0, 7.0, 8.0, and 10.0 mm from top to bottom. The corresponding EWAMs were $Fe_{70}Co_{30}$, $Fe_{65}Co_{30}Cu_5$, $Fe_{60}Co_{30}Cu_{10}$, and $Fe_{50}Co_{30}Cu_{20}$ foam, respectively. Due to the presence of the PEC backing, all incident EM waves are reflected, and thus the EM absorption performance can be directly evaluated from the reflection coefficient[3]:

$$RL\ (dB)=20\log_{f_0}|S_{11}| \quad (6)$$

RESULTS AND DISCUSSION

Theoretical construction optimized EM parameters

Achieving broadband EM wave absorption with a single-layer homogeneous EWAM backed by a metal plate with a relatively small coating thickness (≤ 2.0 mm) remains a critical challenge. Conventional strategies primarily rely on empirical optimization of composition and microstructure, lacking direct theoretical guidance. In practical design, the EM wave absorption performance is typically evaluated by applying transmission line theory to the measured complex permittivity and permeability, which inherently leads to an empirical correlation between frequency-dependent EM parameters and EABs. However, if the functional relationship between the optimal EM parameters and the thickness-frequency combination can be established, EMAMs design can be rationally guided by tuning the EM parameters toward this target relationship, which is of great significance for the development of broadband EWAMs. The RL values of EWAMs are governed by the ε_r and μ_r (Equation 1 and 2). For simplification, the magnetic contribution was neglected (μ_r = 1.00-0.00j)), allowing the determination of the required ε_r' and ε_r'' that minimize RL values at given coating thicknesses and frequencies. As shown in Figure 1A and Figure 1B, the extracted permittivity distributions lead to RL values below -40.00 dB across multiple thicknesses (1.50, 1.75, and 2.00 mm), indicating nearly ideal EM absorption performance [Figure 1C]. To gain further insight into the governing mechanism, two characteristic parameters were introduced, defined as:

$$C_1 = fd\sqrt{\varepsilon_r'} \quad (7)$$

$$C_2 = fd\varepsilon_r'' \quad (8)$$

Remarkably, both C_1 and C_2 remain nearly constant with respect to frequency [Figure 1D and Figure 1E], with values of approximately 76 and 95, respectively. This observation suggests that the optimal permittivity follows the relationships:

$$\varepsilon_r' = \left(\frac{76}{fd}\right)^2 \quad (9)$$

$$\varepsilon_r'' = \frac{95}{fd} \quad (10)$$

Under this condition, excellent EM absorption performance is expected over a wide frequency range.

To validate this hypothesis, the permittivity was constrained to satisfy the above relations at 1.50, 1.75, and 2.00 mm, with (μ_r' = 1.00) and (μ_r'' = 0.00). The calculated RL values remain below -20.00 dB across the entire frequency range, confirming the robustness of the proposed relationship [Figure 1F]. Furthermore, the universality of this model was examined by extending the thickness to 1.00-3.00 mm (step: 0.25 mm). The corresponding permittivity distributions [Supplementary Figure 1A and Supplementary Figure 1B] and RL curves [Supplementary Figure 1C] demonstrate consistently strong absorption, indicating that the proposed functional form provides a reliable guideline for broadband absorber design.

To gain physical insight into this parameter construction, the effective electrical thickness was analyzed using[34]:

$$d_e = \frac{2\pi d}{\lambda} \tag{11}$$

$$\lambda = \frac{c}{f\sqrt{\varepsilon_r \mu_r}} \tag{12}$$

Figure 1G shows the electrical thickness calculated from the constructed permittivity defined by Equations (9) and (10), whereas Figure 1H shows the electrical thickness recalculated from the RL-minimized permittivity extracted at each frequency-thickness point. The consistency between these two results confirms that the constructed parameter relationship captures the near-quarter-wavelength condition required for optimal absorption. As shown in Figure 1G, the electrical thickness remains nearly constant and is centered around $\frac{\pi}{2}$, corresponding to approximately a quarter-wavelength condition. This indicates that the quarter-wavelength destructive interference condition is approximately satisfied over a wide range of frequencies and thicknesses, enabling quasi-scale-invariant impedance matching[35]. In addition, the dielectric loss tangent ($\tan\delta_e$) follows:

$$\tan\delta_e=\frac{\varepsilon_r''}{\varepsilon_r'}=0.0164\,fd \quad (13)$$

which increases linearly with the product of f and d. This implies that at higher frequencies or larger thicknesses, the dielectric loss is automatically enhanced, ensuring sufficient attenuation to suppress multiple reflections from the metallic backing. Essentially, the proposed functional form realizes a normalization of frequency and thickness, allowing both impedance matching and attenuation to approach optimal conditions simultaneously over a broad parameter space. Further calculations reveal that the electrical thickness corresponding to optimal absorption remains consistently close to $\frac{\pi}{2}$ across different thicknesses [Figure 1H], while the normalized loss parameter $\tan\delta_e/(fd)$ fluctuates narrowly around 0.0164 [Figure 1I]. These results collectively validate the physical rationality of the proposed parameter construction.

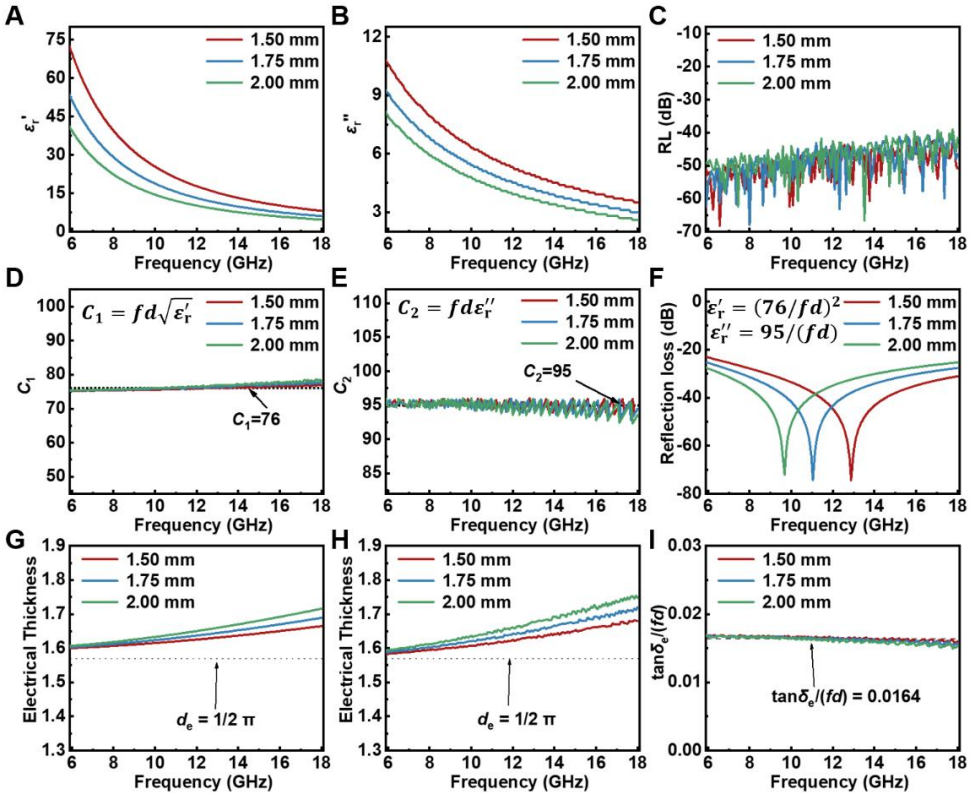

Figure 1. Theoretical determination of optimal permittivity for broadband EM wave absorption based on transmission line theory. (A) ε_r', and (B) ε_r'' as a function of frequency with different coating thicknesses (1.50, 1.75, and 2.00 mm); (C) Corresponding RL values calculated using the extracted permittivity. Frequency

dependence of the parameter (D) C_1; and (E) C_2; (F) Simulated RL values using the constructed optimal permittivity; (G) Electrical thickness calculated from the constructed permittivity defined by Equations (9) and (10); (H) Electrical thickness, and (I) normalized dielectric loss factor recalculated from the RL-minimized permittivity extracted at each frequency-thickness point.

Bandwidth limitation of single loss mechanism

Although the optimal permittivity required for broadband absorption has been theoretically established, it remains highly challenging to realize such a functional relationship through practical material design. This difficulty arises from the fact that the frequency-dependent permittivity is fundamentally governed by intrinsic loss mechanisms, which can generally be classified into conduction loss and polarization loss[36-38]. Importantly, the frequency dependence associated with these mechanisms is inherently fixed and deviates from the idealized permittivity-frequency relationship derived above. For conduction-dominated EWAMs, the dielectric response originates from leakage currents and can be equivalently described by an ideal capacitor in parallel with a resistor. In this case, the real part of permittivity remains constant, determined by the charge storage capability, while the imaginary part follows an inverse frequency dependence governed by the electrical conductivity (Equation 3). Here, k denotes the frequency-independent ε_r' in the pure conduction-loss model, and is used together with electrical conductivity to evaluate the bandwidth limitation of conduction-dominated EWAMs. The EABs as a function of permittivity and conductivity with coating thicknesses of 1.50, 1.75, and 2.00 mm are presented in Figure 2A-C. It is evident that, regardless of increasing the permittivity or conductivity, the effective bandwidth exhibits a clear upper limit. Although increasing coating thickness can extend this limit, the maximum EAB remains below 5.0 GHz with a coating thickness of 2.0 mm. This indicates that conduction loss alone is insufficient to achieve broadband absorption under thin-layer conditions.

When the dielectric response is dominated by polarization loss, the permittivity can be described by the Debye relaxation model (Equation 4 and 5), where ε_∞, ε_s-ε_∞, and τ represents the high-frequency permittivity limit, relaxation strength, and relaxation time, respectively. The corresponding EABs under different parameter combinations are shown in Figure 2D-F. For thicknesses of 1.50, 1.75, and 2.00 mm, the maximum EABs

are 5.25, 5.97, and 6.60 GHz, respectively, achieved at (ε_∞, ε_s-ε_∞, τ) = (5.8, 11.2, 10.8 ps), (4.2, 10.3 ,12.2 ps), and (3.1, 9.5, 12.8 ps). These results clearly demonstrate that polarization loss, owing to its additional tunable parameters, provides a higher upper limit of EABs compared to pure conduction loss.

The introduction of magnetic components can further improve impedance matching characteristics and simultaneously introduce additional magnetic loss mechanisms, such as eddy current loss and ferromagnetic resonance to further broaden the upper limit of EABs[37-39]. Therefore, EWAMs with combined dielectric and magnetic losses are expected to exhibit superior broadband absorption performance compared to purely dielectric systems[40]. To verify this hypothesis, the relative permeability was artificially set to μ_r' =1.2 and μ_r'' = 0.2, and the above calculations were repeated. As shown in Figure 2G-I, the maximum EAB is further enhanced to 6.20, 7.08, and 7.88 GHz with coating thicknesses of 1.50, 1.75, and 2.00 mm, respectively. The corresponding optimal parameters are (5.1, 9.3, 10.1 ps), (4.0, 8.8, 11.9 ps), and (3.3, 8.6 ,13.9 ps).

These results collectively indicate that neither conduction loss nor polarization loss alone can fully satisfy the requirements for thin-layer broadband absorption. Instead, the synergistic combination of conduction loss, polarization loss, and magnetic loss is essential to approach the theoretically optimal absorption condition. This also highlights the necessity of designing EWAMs with multi-mechanism loss coupling to bridge the gap between ideal permittivity construction and practical realization.

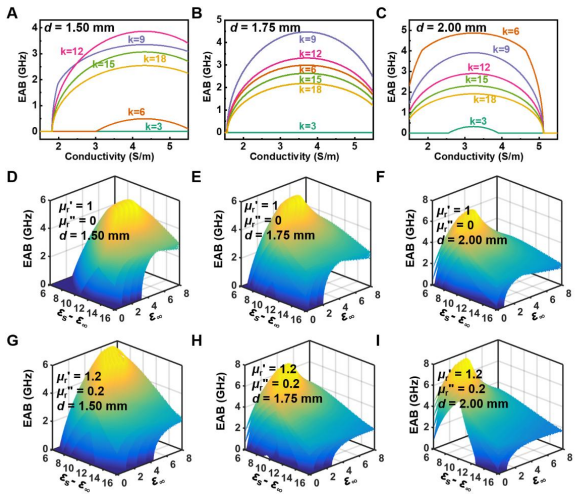

Figure 2. EAB maps of conduction-loss-dominated EWAMs as functions of electrical

conductivity σ and the constant real permittivity k ($\varepsilon_r' = k$) with coating thicknesses of (A) 1.50; (B) 1.75, and (C) 2.00 mm, respectively. Three-dimensional maps of EABs as a function of ε_∞, ε_s-ε_∞, and τ for polarization-loss-dominated materials with coating thicknesses of (D) 1.50; (E) 1.75, and (F) 2.00 mm, respectively; Corresponding EAB distributions after introducing magnetic loss (μ_r' =1.2 and μ_r'' = 0.2) with coating thicknesses of (G) 1.50; (H) 1.75; and (I) 2.00 mm, respectively.

Although the ideal permittivity-frequency-thickness relationship defines a clear target for broadband absorption, it represents a theoretical constraint rather than a directly attainable material property. Achieving such behavior in practice requires precise regulation of composition, phase structure, and microstructure[41]. As indicated by the preceding analysis, broadband absorption under thin-layer conditions relies on tailoring the dielectric response toward the optimal parameter distribution, while introducing appropriate magnetic contributions to further expand the effective bandwidth[42]. Based on this rationale, FeCoCu foams were selected as a model system to validate the proposed design strategy. FeCo-based alloys inherently exhibit strong dielectric and magnetic losses, providing a robust foundation for EM attenuation[43]. The introduction of Cu is expected to regulate conduction loss by modifying charge transport and conductive pathways, while phase separation during alloy formation generates abundant heterogeneous interfaces that promote interfacial polarization and dipolar relaxation[44]. Consequently, the FeCoCu system offers an ideal platform for the synergistic coupling of conduction, polarization, and magnetic losses.

Synthesis and characterization of FeCoCu alloy foam

FeCoCu alloy foams were synthesized via a nitrate-glycine-assisted solution combustion method followed by reduction [Figure 3A]. This process enables homogeneous precursor mixing and rapid gas evolution, resulting in a three-dimensional interconnected porous framework. The oxide precursors exhibit typical foam-like architectures with highly open and interconnected pores [Figure 3B and Supplementary Figure 2A-C], arising from intense gas release during combustion. After reduction, the overall foam morphology is preserved, while the skeleton evolves into a rough, nanoparticle-assembled structure [Figure 3C and Supplementary Figure 2D-F]. This hierarchical architecture, combining microscale channels with nanoscale building units, enhances multiple scattering and provides abundant interfacial sites for

polarization. TEM and elemental mapping [Figure 3D] confirm the uniform distribution of Fe, Co, and Cu within interconnected nanoparticles, while local contrast variations suggest nanoscale compositional fluctuations. Such heterogeneity likely leads to FeCo-rich and Cu-rich domains, forming interfacial regions that facilitate Maxwell-Wagner polarization.

XRD results [Figure 3E] reveal a transition from a single BCC phase in $Fe_{70}Co_{30}$ to a BCC/FCC dual-phase structure with increasing Cu content, consistent with limited Cu solubility and its tendency to induce phase separation[45,46]. The emergence of dual phases introduces additional interfaces, enhancing polarization loss. Meanwhile, the systematic peak shift from 44.84° to 45.05° [Figure 3F] indicates lattice modulation and increased structural distortion, further contributing to dielectric loss.

ICP analysis [Figure 3G] confirms the effective compositional control, with Cu content increasing from 0 to 19.4 wt.% and Fe correspondingly decreasing, while Co remains nearly constant. This compositional tunability enables systematic investigation of structure-property relationships. Mercury intrusion results [Figure 3H and 3I] show that, although partial densification occurs during reduction (intrusion volume decreasing from 3.7 to 2.3 mL/g), the hierarchical pore structure is largely retained. The resulting multiscale porosity simultaneously favors impedance matching and enhances multiple scattering, while the metallic framework supports conduction loss. Magnetic measurements [Figure 3J] indicate typical soft ferromagnetic behavior. The saturation magnetization decreases from 208.4 to 166.7 emu/g with increasing Cu content due to magnetic dilution, while coercivity increases from 105.6 to 177.0 Oe, reflecting structural evolution and enhanced anisotropy. Despite reduced magnetization, all samples retain sufficient magnetic response to support resonance-based magnetic losses, which are critical for impedance matching and bandwidth expansion.

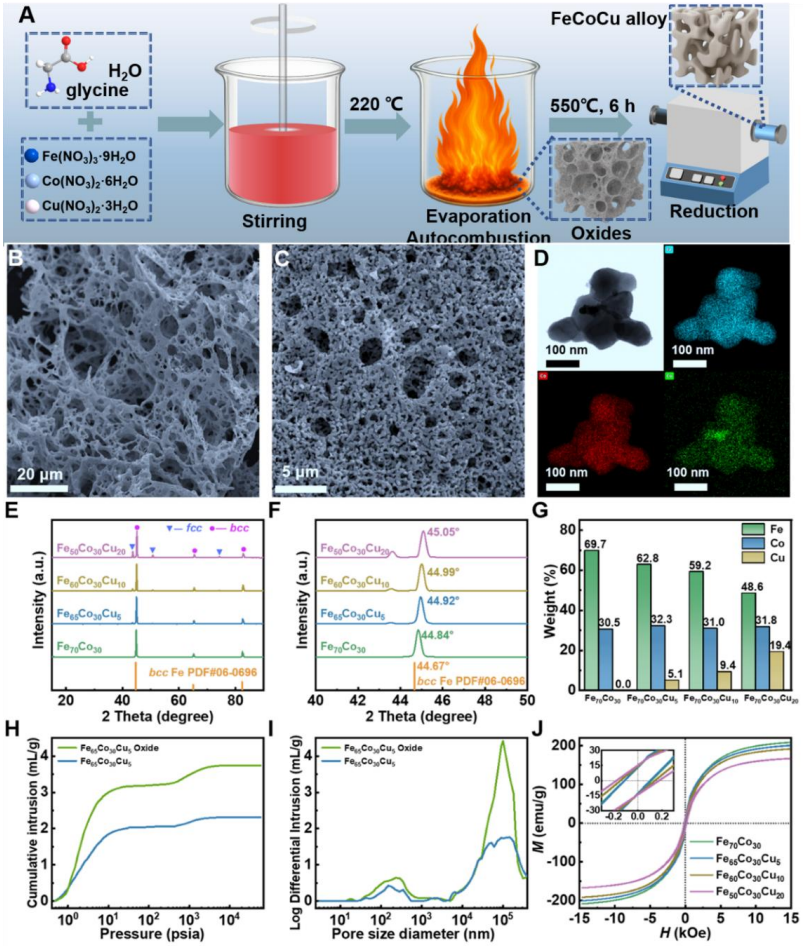

Figure 3. Synthesis process, struct ural evolution, and physicochemical characterization of FeCoCu alloy foams with different Cu contents. (A) Schematic illustration of the synthesis process. SEM images of (B) the $Fe_{65}Co_{30}Cu_5$ oxide precursor, and (C) corresponding reduced $Fe_{65}Co_{30}Cu$ alloy; (D) TEM image $Fe_{65}Co_{30}Cu$ alloy and corresponding elemental mappings of Fe, Co, and Cu; (E) XRD patterns of FeCoCu alloys with varying Cu contents, and (F) corresponding enlarged XRD patterns in the 40-50° range; (G) ICP-derived elemental compositions of FeCoCu alloys with varying Cu contents; (H) Mercury intrusion cumulative pore volume curves of $Fe_{65}Co_{30}Cu_5$ oxide precursor and reduced alloy; and (I) corresponding pore size distributions; (j) Magnetic hysteresis loops of FeCoCu alloys with varying Cu contents.

Overall, FeCoCu foams achieve a synergistic regulation of composition, phase structure, and hierarchical porosity. Cu incorporation not only drives the BCC-to-BCC/FCC transition and increases interfacial density, but also introduces structural heterogeneity that enhances polarization loss. Combined with the three-dimensional porous framework and retained magnetic response, these features provide an integrated

platform for tuning conduction, polarization, and magnetic losses. This synergy is essential for approaching the theoretically optimal absorption condition and enables efficient broadband EM wave absorption under thin-layer constraints.

Dielectric and magnetic loss behaviors of FeCoCu foam

To further elucidate the EM loss mechanisms and their composition dependence in FeCoCu foams, the complex ε_r, μ_r, and corresponding loss factors were systematically analyzed. As shown in Figure 4A and 4B, all samples exhibit pronounced frequency dispersion in the range of 2.00-18.00 GHz, with clear composition-dependent evolution. Specifically, both the ε_r' and ε_r'' increase markedly with increasing Cu content. The $Fe_{70}Co_{30}$ sample shows relatively low ε_r', decreasing from 6.0 to 4.8, whereas $Fe_{65}Co_{30}Cu_5$ and $Fe_{60}Co_{30}Cu_{10}$ exhibit higher and more stable values (8.0-10.5). Further increasing Cu to 20 at.% results in a substantial enhancement of ε_r', indicating significantly improved charge storage. A similar trend is observed for ε_r'', where $Fe_{50}Co_{30}Cu_{20}$ maintains the highest values across the entire frequency range, confirming its strong energy dissipation capability. The $\tan\delta_e$ values [Supplementary Figure 3] follow the same trend as ε_r'', increasing with Cu content. $Fe_{70}Co_{30}$ exhibits negligible loss, while $Fe_{65}Co_{30}Cu_5$ and $Fe_{60}Co_{30}Cu_{10}$ show moderate values. In contrast, $Fe_{50}Co_{30}Cu_{20}$ reaches significantly higher levels, indicating more efficient EM energy dissipation. However, excessive dielectric loss may deteriorate impedance matching due to overly strong dielectric responses, implying that optimal EM wave absorption requires a balance between EM attenuation capability and impedance matching rather than maximizing EM loss alone.

According to the Debye relaxation model and free electron theory, the imaginary permittivity can be expressed as the sum of conduction and polarization contributions[38,47]:

$$\varepsilon_r''=\varepsilon_c''+\varepsilon_p''=\frac{\sigma}{2\pi f\varepsilon_0}+\frac{2\pi f\tau(\varepsilon_s-\varepsilon_\infty)}{1+(2\pi f\tau)^2} \quad (14)$$

By fitting the experimental ε_r'' data using a least-squares method, the conduction loss component ε_c'' and polarization contribution ε_p'' were separated [Figure 4C and 4D]. As shown in Figure 4C, ε_c'' decreases with increasing frequency and increases significantly

with Cu content. The $Fe_{70}Co_{30}$ sample exhibits negligible conduction loss, whereas the Cu-containing samples show progressively enhanced contributions, indicating improved electron transport. This is consistent with the electrical conductivity results [Figure 4E], where conductivity increases from 0.02 to 1.01 S/m with increasing Cu content. Nevertheless, conduction loss alone cannot fully account for the observed dielectric behavior. As shown in Figure 4D, significant polarization loss remains after subtracting the conduction contribution, and this component also increases with Cu content. $Fe_{70}Co_{30}$ shows weak polarization, while $Fe_{65}Co_{30}Cu_5$ and $Fe_{60}Co_{30}Cu_{10}$ exhibit more pronounced fluctuations. The $Fe_{50}Co_{30}Cu_{20}$ sample shows the strongest and most complex polarization behavior, with multiple peaks indicating active and diverse relaxation processes. This enhancement of polarization loss is closely associated with crystal structure evolution. As revealed by XRD analysis, increasing Cu content induces a transition from a single BCC phase to a BCC/FCC dual-phase structure, significantly increasing the density of heterogeneous interfaces. In addition, alloying-induced compositional fluctuations, lattice distortion, defects, and particle-particle contacts further contribute to interfacial charge accumulation under alternating EM fields, leading to Maxwell-Wagner polarization. The hierarchical porous structure, combined with nanoscale heterogeneity, further promotes dipolar relaxation[48]. Therefore, the role of Cu extends beyond improving conductivity—it fundamentally enhances polarization by introducing structural heterogeneity and interfacial complexity, enabling the synergistic coupling of conduction and polarization losses.

To further investigate relaxation behavior, Cole-Cole plots were constructed from ε_r' and ε_r'' [Supplementary Figure 4A-D]. According to classical Debye theory, a single relaxation process corresponds to a perfect semicircle, whereas multiple semicircles, distorted arcs, and tailing features indicate the coexistence of multiple relaxation processes and conduction effects. All samples exhibit multiple semicircles and distorted arcs, confirming that FeCoCu foams involve complex and multi-scale relaxation processes rather than a single Debye relaxation. This further supports the conclusion that broadband dielectric loss in this system originates from the cooperative contribution of conduction loss, interfacial polarization, and dipolar relaxation.

To more intuitively quantify the synergistic evolution of conduction and polarization losses induced by Cu incorporation, an equivalent circuit model [Supplementary Figure

5] was employed to describe EWAMs that simultaneously exhibit conduction and polarization dissipation.[49] In this model, the parallel branch represents conduction loss dominated by free electron transport, while the series branch accounts for polarization loss associated with dipolar relaxation and interfacial polarization. By establishing a correspondence between the complex permittivity of the equivalent circuit and the modified Debye model, the frequency-dependent EM response can be transformed into physically meaningful circuit parameters, including the parallel conductivity (σ_1), parallel capacitance (ε_1), series conductivity (σ_2), and series capacitance (ε_2).

The equivalent complex permittivity of the circuit can be expressed as[50,51]:

$$j\omega\varepsilon_0\varepsilon_r=\sigma_1+j\omega\varepsilon_1+\frac{1}{\frac{1}{\sigma_2}+\frac{1}{j\omega\varepsilon_2}} \quad (15)$$

which can be rearranged into:

$$\varepsilon_r=\left[\frac{\varepsilon_1}{\varepsilon_0}+\frac{\frac{\varepsilon_2}{\varepsilon_0}}{1+\left(\frac{\omega\varepsilon_2}{\sigma_2}\right)^2}\right]-j\left[\frac{\sigma_1}{\omega\varepsilon_0}+\frac{\frac{\varepsilon_2}{\varepsilon_0}\left(\frac{\omega\varepsilon_2}{\sigma_2}\right)}{1+\left(\frac{\omega\varepsilon_2}{\sigma_2}\right)^2}\right] \quad (16)$$

According to the modified Debye relaxation model, the complex permittivity can also be written as:

$$\varepsilon_r=\left[\varepsilon_\infty+\frac{\varepsilon_s-\varepsilon_\infty}{1+(\omega\tau)^2}\right]-j\left[\frac{\sigma}{\omega\varepsilon_0}+\frac{(\varepsilon_s-\varepsilon_\infty)\omega\tau}{1+(\omega\tau)^2}\right] \quad (17)$$

By comparing Equation 16 and Equation 17, the following relationships can be obtained:

$$\varepsilon_1=\varepsilon_\infty\varepsilon_0 \quad (18)$$

$$\varepsilon_2=(\varepsilon_s-\varepsilon_\infty)\varepsilon_0 \quad (19)$$

$$\sigma_1=\sigma \quad (20)$$

$$\sigma_2=\frac{(\varepsilon_s-\varepsilon_\infty)\varepsilon_0}{\tau} \quad (21)$$

Therefore, once σ, ε_∞, ε_s- ε_∞, and τ are determined, the corresponding equivalent circuit

parameters can be quantitatively calculated. The conductivity σ was obtained from dielectric decomposition [Figure 4E], while ε_s and ε_∞ were extracted from Cole-Cole semicircles based on Debye theory[52,53]:

$$\left[\varepsilon_r' - \frac{\varepsilon_s+\varepsilon_\infty}{2}\right]^2 + (\varepsilon_r'')^2 = \left(\frac{\varepsilon_s-\varepsilon_\infty}{2}\right)^2 \quad (22)$$

By analyzing the center and radius of the semicircle, $\varepsilon_s + \varepsilon_\infty$ and $\varepsilon_s - \varepsilon_\infty$ can be determined, from which ε_∞ and $\varepsilon_s - \varepsilon_\infty$ are obtained. As shown in Figure 4F and Supplementary Figure 6A, $\varepsilon_s + \varepsilon_\infty$ increases from 11.07 to 26.28 with increasing Cu content, while $\varepsilon_s - \varepsilon_\infty$ increases significantly from 0.32 to 3.58, indicating a substantial enhancement of polarization strength. Furthermore, since the Debye relaxation term reaches its maximum at $\omega\tau = 1$, the relaxation time τ can be determined accordingly. The characteristic τ values for $Fe_{70}Co_{30}$, $Fe_{65}Co_{30}Cu_5$, $Fe_{60}Co_{30}Cu_{10}$, and $Fe_{50}Co_{30}Cu_{20}$ are 11.84, 11.73, 11.76, and 11.88 ps, respectively [Supplementary Figure 6B], showing negligible variation. The equivalent circuit parameters are summarized in Table 1.

From the parallel branch perspective, σ_1 increases monotonically from 0.02 to 1.01 S/m with increasing Cu content, indicating a continuous enhancement of charge transport and conduction loss. This behavior originates from both the intrinsically high conductivity of Cu and the improved connectivity of conductive pathways, reduced transport barriers, and enhanced particle contact within the porous framework. Meanwhile, ε_1 increases from 47.59 to 100.49 pF/m, suggesting a strengthened high-frequency dielectric response and enhanced energy storage capability. More importantly, the series branch parameters exhibit a much stronger increase. The polarization-related capacitance ε_2 rises sharply from 2.83 to 31.70 pF/m, while σ_2 increases from 0.24 to 2.67 S/m. Given that τ remains nearly constant (11.8 ps), this enhancement is primarily attributed to the increase in $\varepsilon_s - \varepsilon_\infty$ rather than changes in relaxation dynamics. This indicates that Cu incorporation does not introduce new relaxation mechanisms but amplifies existing ones by increasing the density and strength of polarization-active sites. Notably, the increase in ε_2 and σ_2 is significantly more pronounced than that of σ_1 and ε_1, especially at high Cu content. This suggests that polarization loss is more sensitive to Cu incorporation than conduction loss. Such behavior is closely related to structural evolution: Cu induces a transition from a single

BCC phase to a BCC/FCC dual-phase system, increasing interfacial density, compositional heterogeneity, and defect concentration. These features promote Maxwell-Wagner interfacial polarization and dipolar relaxation, thereby significantly enhancing dielectric loss. The nearly invariant τ further indicates that the dominant polarization mechanism remains fundamentally unchanged. Instead, Cu enhances dielectric loss primarily by amplifying polarization intensity rather than shifting relaxation frequency.

In addition to dielectric behavior, the magnetic response also shows clear composition dependence. As shown in Figure 4G, μ_r' values decrease with increasing Cu content due to magnetic dilution, while μ_r'' values [Figure 4H] remains in the range of 0.1-0.6 and exhibits frequency-dependent fluctuations, indicating multiple magnetic loss mechanisms. The magnetic loss factor ($\tan\delta_m$, Supplementary Figure 7) remains within a moderate range (0.1-0.4), suggesting that although Cu reduces overall magnetization, sufficient magnetic dissipation is retained. This moderate and frequency-selective magnetic loss is beneficial for improving impedance matching. To further clarify the magnetic loss mechanism, the eddy current coefficient was calculated[54,55]:

$$C_0=\mu_r''(\mu_r')^{-2}f^{-1} \quad (23)$$

As shown in Figure 4I, C_0 is not constant with frequency, indicating that magnetic loss is not solely governed by eddy current effects but involves natural resonance and exchange resonance.

Overall, Cu incorporation induces a synergistic enhancement of conduction, polarization, and magnetic losses. While conductivity increases strengthen conduction loss, the formation of heterogeneous interfaces significantly amplifies polarization loss. Meanwhile, sufficient magnetic loss is preserved despite partial magnetic dilution. Therefore, the FeCoCu system achieves a cooperative coupling of multiple loss mechanisms, which is essential for realizing broadband electromagnetic wave absorption.

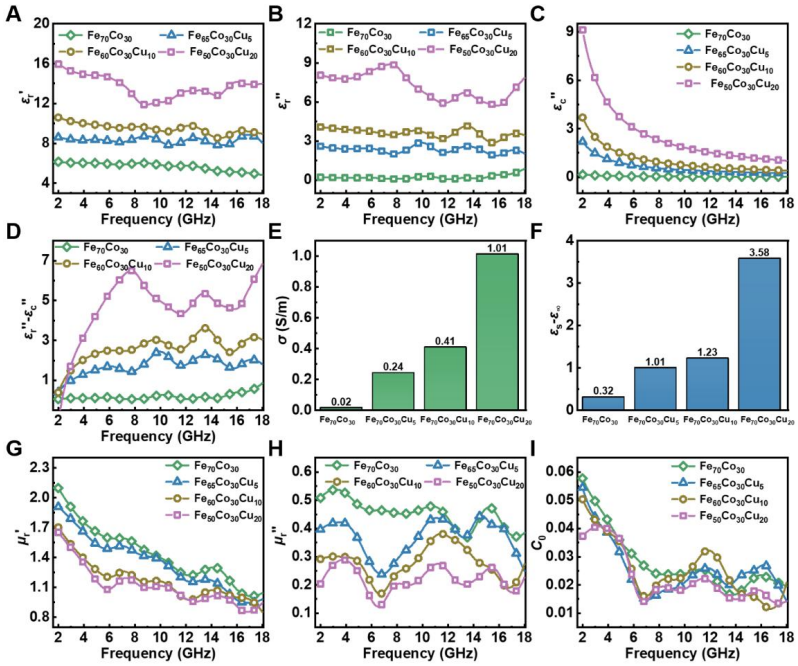

Figure 4. Composition-dependent EM parameters and dielectric loss mechanism decomposition of FeCoCu foams. (A) ε_r' values; (B) ε_r" values; (C) ε_c" values extracted from ε_r"; and (D) ε_r"-ε_c" values of FeCoCu foams with various Cu contents; (E) Electrical conductivity values, and (F) ε_s-ε_∞ values of FeCoCu foams with various Cu contents derived from dielectric analysis. (G) μ_r' values; (H) μ_r" values, and (I) C0 values of FeCoCu foams with various Cu contents.

Table 1. Equivalent circuit parameters of FeCoCu alloys with different Cu contents.

	$Fe_{70}Co_{30}$	$Fe_{65}Co_{30}Cu_5$	$Fe_{60}Co_{30}Cu_{10}$	$Fe_{50}Co_{30}Cu_{20}$
σ_1 (S/m)	0.02	0.24	0.41	1.01
ε_1 (pF/m)	47.59	68.40	75.97	100.49
σ_2 (S/m)	0.24	0.76	0.93	2.67
ε_2 (pF/m)	2.83	8.94	10.89	31.70

EM absorption performance and loss mechanism analysis

Further evaluation of the EM wave absorption performance of FeCoCu alloy foams with different Cu contents was conducted, as shown in Figure 5. The three-dimensional reflection loss maps reveal that the Cu content plays a decisive role in determining the absorption behavior. The $Fe_{70}Co_{30}$ sample exhibits a minimum reflection loss of -20.8 dB [Figure 5A], indicating a certain absorption capability, although both the absorption

intensity and bandwidth remain limited. After introducing 5 at.% Cu, the RL_{min} of $Fe_{65}Co_{30}Cu_5$ decreases markedly to -52.9 dB [Figure 5B], demonstrating a substantial improvement in microwave attenuation. When the Cu content is further increased to 10 at.%, $Fe_{60}Co_{30}Cu_{10}$ still maintains strong absorption ability, with an RL_{min} of -26.7 dB [Figure 5C]. However, when the Cu content reaches 20 at.%, the RL_{min} of $Fe_{50}Co_{30}Cu_{20}$ increases to only -11.8 dB [Figure 5D], indicating a significant deterioration of absorption performance. These results suggest that Cu incorporation is not monotonically beneficial. Although excessive Cu can enhance dielectric loss, it may simultaneously weaken magnetic loss and induce impedance mismatch, thereby suppressing the penetration of incident electromagnetic waves into the absorber. The two-dimensional reflection loss maps further clarify the differences in EABs among the samples. $Fe_{70}Co_{30}$ achieves a maximum EAB of 5.36 GHz with coating thickness of 2.18 mm [Figure 5E], whereas $Fe_{65}Co_{30}Cu_5$ delivers the widest bandwidth of 7.36 GHz with coating thickness of only 1.74 mm [Figure 5F], exhibiting the best broadband absorption performance. $Fe_{60}Co_{30}Cu_{10}$ also maintains a considerable effective bandwidth of 6.00 GHz with coating thickness of 1.67 mm [Figure 5G]. In contrast, $Fe_{50}Co_{30}Cu_{20}$ shows a much narrower maximum effective bandwidth of only 1.36 GHz [Figure 5H]. Combined with the preceding electromagnetic parameter analysis, these results indicate that an appropriate Cu content can simultaneously enhance conduction loss and interfacial polarization loss while preserving sufficient magnetic loss. In contrast, excessive Cu leads to overly strong dielectric response and weakened magnetic response, resulting in severe impedance mismatch and enhanced surface reflection, thereby limiting broadband absorption.

To further elucidate the origin of these performance differences, the attenuation capability (α), input impedance characteristics (η_{in}), interference loss ($E_{1/4\lambda}$), and total energy dissipation ($E_{total\ loss}$), which can be calculated using the following equations[29,36,56-58].

$$\alpha=\frac{\sqrt{2}\pi f}{c}\sqrt{(\mu_r''\varepsilon_r''-\mu_r'\varepsilon_r')+\sqrt{(\mu_r''\varepsilon_r''-\mu_r'\varepsilon_r')^2+(\mu_r''\varepsilon_r'+\mu_r'\varepsilon_r'')^2}} \quad (24)$$

$$\eta_{in}=\sqrt{\frac{\mu_r}{\varepsilon_r}} \quad (25)$$

$$T=\exp(-2j\pi fd\sqrt{\mu_r\varepsilon_r}/c) \quad (26)$$

$$\Pi=\frac{-(1-\Gamma^2)T^2}{1-\Gamma T^2} \quad (27)$$

$$E_{loss}=1-|\Gamma|^2-|T|^2 \quad (28)$$

$$E_{1/4\lambda}=2|\Gamma\Pi|\cos(\pi-\phi) \quad (29)$$

$$E_{total\ loss}=E_{loss}+E_{1/4\lambda} \quad (30)$$

where the factor T reflects the attenuation of the EM wave, Π represents reflection at the metal backplate, and ϕ is the phase difference between Π and Γ. As shown in Figure 5I, the attenuation constant increases with increasing Cu content, and $Fe_{50}Co_{30}Cu_{20}$ exhibits the highest attenuation capability, suggesting the strongest conductive and polarization losses. However, strong attenuation alone does not necessarily guarantee superior absorption performance. Figure 5J shows that the input impedance decreases with increasing Cu content, indicating that high-Cu samples possess a larger impedance difference from free space, which hinders the effective entry of incident EM waves into the EWAM. Therefore, although $Fe_{50}Co_{30}Cu_{20}$ exhibits the strongest attenuation, its poor impedance matching results in the weakest actual absorption performance.

The interference loss contribution shown in Figure 5K further confirms the importance of the quarter-wavelength cancellation condition in determining the absorption peak position and effective bandwidth. $Fe_{65}Co_{30}Cu_5$ and $Fe_{60}Co_{30}Cu_{10}$ exhibit relatively favorable interference loss contributions over a broad frequency range, indicating that their EM parameters and matching thicknesses are closer to the ideal absorption conditions proposed in the theoretical analysis[59]. The total energy loss contribution in Figure 5L further demonstrates that $Fe_{65}Co_{30}Cu_5$ and $Fe_{60}Co_{30}Cu_{10}$ can both achieve high energy dissipation in the middle- and high-frequency regions. Among them, $Fe_{65}Co_{30}Cu_5$ achieves the best balance among strong attenuation, impedance matching, and destructive interference, thereby yielding the lowest RLmin and the broadest EAB.

Overall, the EM absorption performance of FeCoCu alloy foams is not governed by a single loss mechanism, but by the synergistic effects of conduction loss, polarization loss, magnetic loss, impedance matching, and interference cancellation. An appropriate Cu content enables the construction of a moderate conductive network and abundant heterogeneous interfaces while retaining the magnetic response of the FeCo matrix. Such a balance realizes the coordinated optimization of attenuation capability, impedance matching, and interference loss, which is essential for achieving thin, efficient, and broadband EM wave absorption.

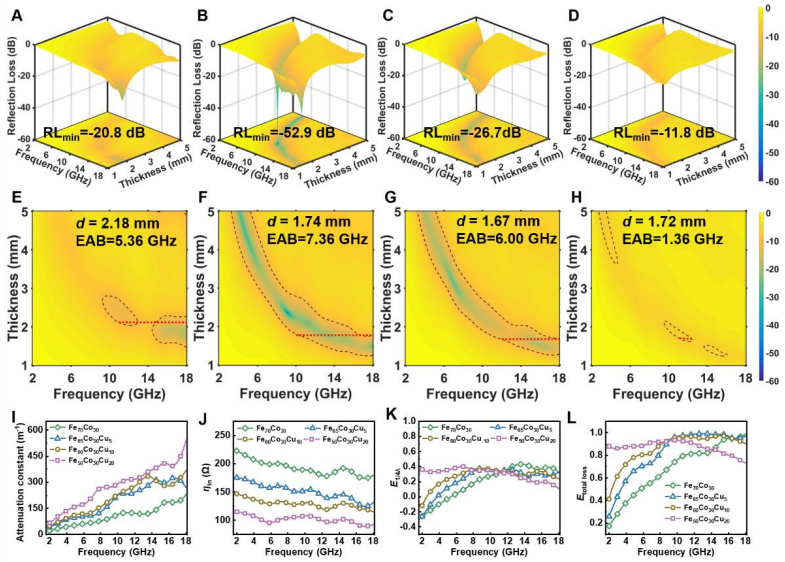

Figure 5. EM wave absorption performance and loss mechanism analysis of FeCoCu alloy foams with different Cu contents. Three-dimensional reflection loss maps of (A) $Fe_{70}Co_{30}$; (B) $Fe_{65}Co_{30}Cu_5$; (C) $Fe_{60}Co_{30}Cu_{10}$ and (D) $Fe_{50}Co_{30}Cu_{20}$; respectively. Corresponding two-dimensional reflection loss contour maps of (E) $Fe_{70}Co_{30}$; (F) $Fe_{65}Co_{30}Cu_5$; (G) $Fe_{60}Co_{30}Cu_{10}$ and (H) $Fe_{50}Co_{30}Cu_{20}$, respectively. The dashed contour lines indicate RL = -10 dB, and the maximum EABs are marked in the corresponding panels. Frequency-dependent (I) attenuation constant; (J) input impedance; (K) interference loss contribution; and (l) total energy loss contribution are presented to clarify the EM absorption mechanism.

RCS reduction simulation and multilayer structural design

To further assess the application potential of FeCoCu foams in practical metal-backed stealth scenarios, CST simulations were conducted to evaluate their radar cross-section reduction capability[60,61]. As illustrated in Figure 6A, FeCoCu foams with a thickness of

1.75 mm were coated onto a 1.0 mm-thick PEC layer to construct a metal-backed EM absorbing structure, and the RCS response was analyzed in the frequency range of 2.00-18.00 GHz. Figure 6B shows that the RCS of the bare PEC layer increases with frequency, confirming its strong reflection toward incident EM waves. In contrast, after coating with FeCoCu EM absorbing layers, the RCS values decrease to different extents. Among all samples, $Fe_{65}Co_{30}Cu_5$ exhibits the most pronounced RCS reduction, with values significantly lower than those of the bare PEC layer and other compositions. This result is consistent with the reflection loss analysis, in which $Fe_{65}Co_{30}Cu_5$ exhibits both the lowest RL_{min} and the widest EAB, indicating that its optimized impedance matching and synergistic loss mechanisms can effectively suppress the backscattering of metallic targets. Figure 6C further compares the RCS reduction of the $Fe_{65}Co_{30}0Cu_5$-coated PEC layer with respect to the bare PEC layer, together with the absolute value of the reflection loss at the same thickness. The RCS reduction curve agrees well with the -RL curve in terms of frequency dependence, and both reach their maximum near 13.00-14.00 GHz. This consistency suggests that the absorption peak revealed by the transmission-line model can be effectively translated into practical scattering suppression. In other words, $Fe_{65}Co_{30}Cu_5$ not only exhibits excellent EM absorption performance in the theoretical reflection loss calculation, but also achieves significant RCS reduction in a more realistic electromagnetic scattering model. For comparison, the RCS reduction behaviors of the other FeCoCu-coated PEC structures are shown in Supplementary Figure 8A-C. Their RCS reduction curves also exhibit frequency-dependent trends that generally follow the corresponding -RL curves, confirming that the reflection loss characteristics of these EWAMs are closely related to their scattering suppression capability. However, their RCS reduction intensities are weaker than that of $Fe_{65}Co_{30}Cu_5$. $Fe_{70}Co_{30}$ shows limited RCS reduction because of insufficient dielectric attenuation, whereas $Fe_{50}Co_{30}Cu_{20}$ exhibits reduced scattering suppression despite its high attenuation capability, which can be attributed to severe impedance mismatch caused by excessive dielectric loss. $Fe_{60}Co_{30}Cu_{10}$ presents an intermediate behavior, consistent with its moderate absorption performance. These results further demonstrate that effective RCS reduction requires a balanced combination of impedance matching and energy dissipation rather than simply maximizing the loss capability.

The angular RCS distributions further confirm the scattering regulation capability of the EM absorbing coating. Figure 6D shows that the bare PEC layer exhibits strong scattering over different azimuth and elevation angles, especially with a pronounced main scattering lobe along the specular reflection direction. In comparison, after coating with 1.75 mm $Fe_{65}Co_{30}Cu_5$, the overall RCS intensity is greatly reduced, the main scattering lobe is significantly compressed, and the side scattering is also effectively suppressed, as shown in Figure 6E. The three-dimensional RCS patterns of $Fe_{70}Co_{30}$, $Fe_{60}Co_{30}Cu_{10}$, and $Fe_{50}Co_{30}Cu_{20}$ are provided in Supplementary Figure 8D-F. Although these coatings also suppress the scattering intensity relative to the bare PEC layer, their reduction effects are less pronounced than that of $Fe_{65}Co_{30}Cu_5$, further verifying the superior angular scattering suppression capability of the optimally Cu-modulated sample. Figure 6F presents the angular RCS curves at different incident angles. The bare PEC layer shows the strongest scattering near 0°, whereas all FeCoCu-coated structures exhibit different degrees of RCS reduction over a broad angular range. Among them, $Fe_{65}Co_{30}Cu_5$ shows the most obvious scattering suppression under normal and near-normal incidence, indicating that its absorption capability is not limited to frequency-domain optimization but also possesses favorable angular adaptability. Based on the preceding dielectric, magnetic, and impedance analyses, this performance can be attributed to the optimized balance among conduction loss, interfacial polarization loss, and magnetic loss induced by moderate Cu incorporation. Such a balance allows EM waves to enter the EWAMs efficiently while being sufficiently dissipated. In contrast, excessive Cu enhances attenuation capability but tends to cause impedance mismatch, thereby limiting RCS reduction.

On this basis, a multilayer frequency-selective surface structure was further designed to broaden the EM absorption bandwidth, as shown in Figure 6G and Figure 6H. The multilayer unit consisted of a 1.0 mm-thick PEC backing layer and four EM absorbing layers, each with a coating thickness of 1.5 mm. The lateral dimensions of the four EM absorbing layers were 6.0, 7.0, 8.0, and 10.0 mm from top to bottom, respectively. In this structure, FeCoCu foams with different Cu contents were introduced into different layers of the frequency-selective units, enabling each layer to contribute to impedance regulation and energy dissipation in different frequency regions. Because FeCoCu foams with different Cu contents possess distinct dielectric losses, magnetic responses, and impedance matching characteristics, the multilayer configuration can construct a

gradient distribution of EM parameters along the propagation direction. This gradient structure reduces the impedance discontinuity at the air/EWAM interface and promotes broadband synergistic EM absorption through multiple reflections, destructive interference, and multi-mechanism energy dissipation. As shown in Figure 6I, the multilayer frequency-selective structure exhibits an ultrabroad absorption bandwidth, with the RL below -10 dB reaching 11.8 GHz and that below -15 dB still reaching 11.3 GHz, significantly outperforming the single-layer homogeneous EWAMs. This result demonstrates that integrating the composition-dependent EM responses of FeCoCu foams with structural design can overcome the trade-off between impedance matching and loss intensity in a single material system, thereby enabling efficient EM wave absorption over a much wider frequency range. It also further validates the design principle proposed in this work: broadband absorption should not rely solely on high loss, but requires the coordinated optimization of conduction loss, polarization loss, magnetic loss, impedance matching, and interference cancellation.

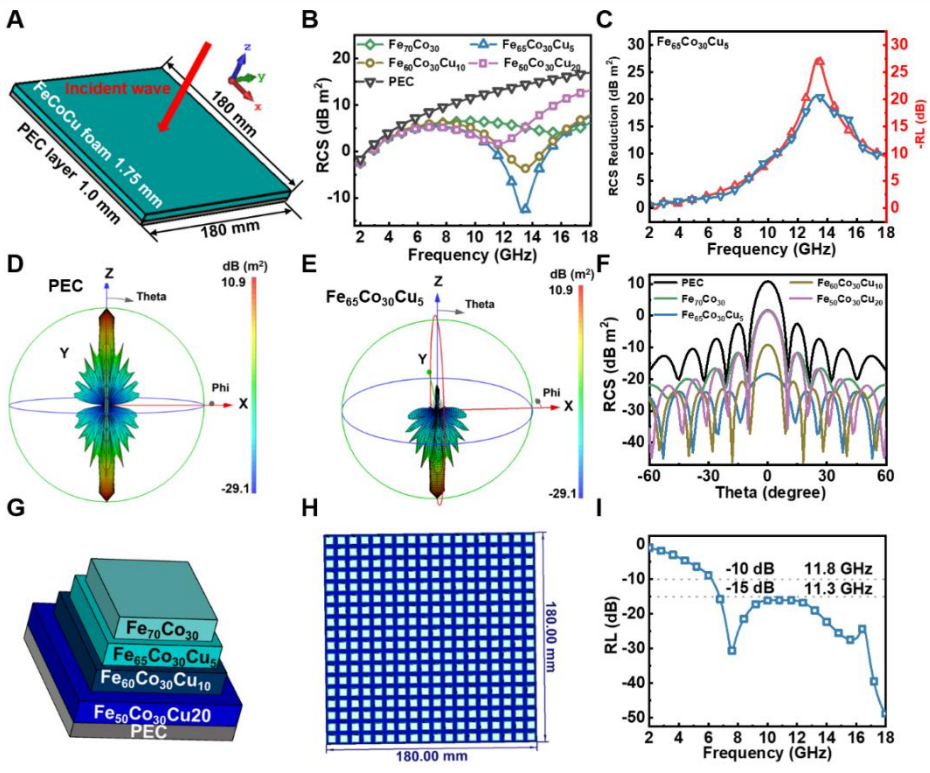

Figure 6. RCS simulation and structural design of FeCoCu-based EWAMs. (A) CST simulation model of FeCoCu foam coated on a PEC layer; (B) RCS values of PEC and FeCoCu-coated PEC layers; (C) RCS reduction of $Fe_{65}Co_{30}Cu_5$-coated PEC compared with bare PEC, together with the corresponding -RL curve; Three-dimensional RCS

patterns of (D) bare PEC; and (E) $Fe_{65}Co_{30}Cu_5$-coated PEC, respectively; (F) Angular RCS distributions of PEC and FeCoCu-coated PEC layers; (G,H) Schematic model of the multilayer frequency-selective structure based on FeCoCu alloys with different Cu contents; (I) Reflection loss curve of the multilayer frequency-selective EWAMs.

CONCLUSIONS

In this work, a theory-guided strategy was proposed to address the challenge of achieving broadband EM wave absorption in thin metal-backed EWAMs. Based on transmission-line theory, the ideal frequency-thickness-dependent permittivity relationship required for broadband absorption was first constructed. Theoretical analysis revealed that excellent absorption can be achieved when the EM parameters simultaneously satisfy appropriate impedance matching, quarter-wavelength cancellation, and sufficient energy attenuation. Further calculations demonstrated that single conduction loss or polarization loss has an intrinsic limitation in bandwidth, whereas the introduction of magnetic response can further broaden the EABs.

Guided by this theoretical framework, FeCoCu alloy foams with tunable Cu contents were designed and synthesized. Structural characterization confirmed that Cu incorporation induced the evolution from a single BCC phase to a BCC/FCC dual-phase structure, generating abundant heterogeneous interfaces while maintaining the porous FeCo-based magnetic framework. EM parameter and equivalent circuit analyses demonstrated that increasing Cu content enhanced both conduction loss and polarization loss, while the FeCo matrix retained considerable magnetic loss. However, excessive Cu caused overly strong dielectric response and impedance mismatch, indicating that high loss alone is insufficient for broadband absorption. Among all samples, $Fe_{65}Co_{30}Cu_5$ exhibited the best balance among attenuation capability, impedance matching, and interference cancellation, achieving a minimum reflection loss of -52.9 dB and an EAB of 7.36 GHz with coating thickness of only 1.74 mm. CST simulations further confirmed its capability for RCS reduction on a PEC substrate. Moreover, a multilayer frequency-selective structure based on FeCoCu foams achieved ultrabroadband absorption, with bandwidths of 11.8 GHz and 11.3 GHz below -10 and -15 dB, respectively. These results verify the effectiveness of combining theoretical EM parameter design with compositional and structural regulation for developing thin, efficient, and broadband EWAMs.

DECLARATIONS

Authors' contributions

Conceptualization, Data curation, Formal analysis, Software, Visualization, Writing-original draft: B.H;

Formal analysis, Investigation, Validation, Software, Writing - original draft: YY.C;

Methodology, Data curation, Resources, Visualization: WK.S;

Methodology, Data curation, Visualization, Resources: YZ.C;

Software, Resources, Investigation: XW;

Supervision, Project administration, Funding acquisition, Formal analysis: XJ.H;

Conceptualization, Formal analysis, Investigation, Supervision, Project administration, Funding acquisition, Writing-review & editing: YC.D.

Availability of data and materials

All data needed to evaluate the conclusions are available in the manuscript and the Supplementary Materials.

AI and AI-assisted tools statement

Not applicable.

Financial support and sponsorship

This work was financially supported by the National Natural Science Foundation of China (No. 22475057 and No. 52373262).

Conflicts of interest

All authors declared that there are no conflicts of interest.

Consent for publication

Not applicable.

REFERENCES

[1] Shi, M. J.; Jia, Z. R.; Lan, D.; et al., Enhanced polarization relaxation of multidimensional bimetallic selenide nanocomposites for electromagnetic wave absorption. *Adv. Funct. Mater.* 2025, *35*, **e02261**.[DOI: 10.1002/adfm.202502261]

[2] Gai, L.; Wang, Y.; Wan, P.; et al., Compositional and hollow engineering of silicon carbide/carbon microspheres as high-performance microwave absorbing materials with good environmental tolerance. *Nano-Micro Lett.* 2024, *16*, **167**.[DOI: 10.1007/s40820-024-01369-6]

[3] Cai, B.; Zhou, L.; Zhao, P.-Y.; et al., Interface-induced dual-pinning mechanism enhances low-frequency electromagnetic wave loss. *Nat. Commun.* 2024, *15*, **3299**.[DOI: 10.1038/s41467-024-47537-5]

[4] He, M.; Zhang, K.; Qiu, H.; et al., Low-frequency microwave absorption composites. *Adv. Sci.* 2025, *12*, **e11580**.[DOI: 10.1002/advs.20251158]

[5] Liang, Q.; He, M.; Zhan, B.; et al., Yolk-shell CoNi@N-doped carbon-CoNi@CNTs for enhanced microwave absorption, photothermal, anti-corrosion, and antimicrobial properties. *Nano-Micro Lett.* 2025, *17*, **167**.[DOI: 10.1007/s40820-024-01626-8]

[6] Shi, Y. X.; Liang, B. Q.; Gao, H.; et al., Research progress on spherical carbon-based electromagnetic wave absorbing composites. *Carbon* 2024, *227*, **119244**.[DOI: 10.1016/j.carbon.2024.119244]

[7] Pan, F.; Pei, K.; Chen, G.; et al., Integrated electromagnetic device with on-off heterointerface for intelligent switching between wave-absorption and wave-transmission. *Adv. Funct. Mater.* 2023, *33*, **2306599**.[DOI: 10.1002/adfm.202306599]

[8] Wang, Y.; Li, X.; Han, X.; et al., Ternary Mo_2C/Co/C composites with enhanced electromagnetic waves absorption. *Chem. Eng. J.* 2020, *387*, **124159**.[DOI: 10.1016/j.cej.2020.124159]

[9] Liu, X.; Zhao, Y.; Zhang, Y.; et al., Bioinspired layered-gradient nanocomposites for intelligent electromagnetic skins with GHz-THz wave absorption, shielding, and solvent-driven actuation. *Nano-Micro Lett.* 2026, *18*, **344**.[DOI: 10.1007/s40820-026-02202-y]

[10] Yang, L. Q.; Wang, Y.; Lu, Z.; et al., Construction of multi-dimensional NiCo/C/CNT/rGO aerogel by MOF derivative for efficient microwave absorption. *Carbon* 2023, *205*, **411-21**.[DOI: 10.1016/j.carbon.2023.01.057]

[11] Wu, L. P.; Gao, H.; Guo, R. H.; et al., MnO_2 intercalation-guided impedance tuning of carbon/polypyrrole double conductive layers for electromagnetic wave absorption.

Chem. Eng. J. 2023, *460*, **141749**.[DOI: 10.1016/j.cej.2023.141749]

[12] Wang, H. W.; Zhang, H.; Zhao, K. Z.; et al., Research progress on electromagnetic wave absorption based on magnetic metal oxides and their composites. *Adv. Compos. Hybrid Mater.* 2023, *6*, **120**.[DOI: 10.1007/s42114-023-00694-5]

[13] Jiang, J.; Lan, D.; Li, Y. Q.; et al., Construction of spherical heterogeneous interface on $ZnFe_2O_4$@C composite nanofibers for highly efficient microwave absorption. *Ceram. Int.* 2024, *50*, **38331-41**.[DOI: 10.1016/j.ceramint.2024.07.197]

[14] Liu, S.; Shen, C.; Deng, Z.; et al., Non-equilibrium pyrolysis enables nano-confined hetero-interfaces in MOF-derivatives for advanced dielectric engineering. *Adv. Funct. Mater.* 2026, **e75267**.[DOI: 10.1002/adfm.75267]

[15] Han, Y.; Guo, H.; Qiu, H.; et al., Multimechanism decoupling for low-frequency microwave absorption hierarchical Fe-doped co magnetic microchains. *Adv. Funct. Mater.* 2025, *35*, **2506803**.[DOI: 10.1002/adfm.202506803]

[16] Xu, Z.; Du, Y.; Liu, D.; et al., Pea-like Fe/Fe_3C nanoparticles embedded in nitrogen-doped carbon nanotubes with tunable dielectric/magnetic loss and efficient electromagnetic absorption. *ACS Appl. Mater. Interfaces* 2019, *11*, **4268-77**.[DOI: 10.1021/acsami.8b19201]

[17] Jia, Z. R.; Sun, L. F.; Gao, Z. G.; Lan, D. Modulating magnetic interface layer on porous carbon heterostructures for efficient microwave absorption. *Nano Res.* 2024, *17*, **10099-108**.[DOI: 10.1007/s12274-024-6939-0]

[18] Chen, N.; Wang, R. Y.; Pan, X. F.; et al., Hollow engineering of core-shell Fe_3O_4@MoS_2 microspheres with controllable interior toward optimized electromagnetic attenuation. *Adv. Compos. Hybrid Mater.* 2025, *8*, **302**.[DOI: 10.1007/s42114-025-01393-z]

[19] Feng, S. X.; Wang, H. W.; Ma, J.; et al., Fabrication of hollow Ni/NiO/C/MnO_2@polypyrrole core-shell structures for high-performance electromagnetic wave absorption. *Compos. Part B Eng.* 2024, *275*, **111344**.[DOI: 10.1016/j.compositesb.2024.111344]

[20] Duan, Y.; Gu, S.; Ma, B.; et al., Metamaterial absorbers with archimedean tiling structures: toward response and absorption of multiband electromagnetic waves. *ACS Appl. Mater. Interfaces* 2024, *16*, **21255-63**.[DOI: 10.1021/acsami.4c03690]

[21] Huang, L.; Duan, Y.; Liu, J.; et al., Bionic composite metamaterials for harvesting of microwave and integration of multifunctionality. *Compos. Sci. Technol.* 2021, *204*, **108640**.[DOI: 10.1016/j.compscitech.2020.108640]

[22] Wei, K. X.; Shi, Y.; Tan, X.; et al., Recent development of metal-organic frameworks and their composites in electromagnetic wave absorption and shielding applications. *Adv. Colloid Interface Sci.* 2024, *332*, **103271**.[DOI: 10.1016/j.cis.2024.103271]

[23] Li, F. S.; Li, Q. Y.; Kimura, H.; et al., Morphology controllable urchin-shaped bimetallic nickel-cobalt oxide/carbon composites with enhanced electromagnetic wave absorption performance. *J. Mater. Sci. Technol.* 2023, *148*, **250-9**.[DOI: 10.1016/j.jmst.2022.12.003]

[24] Liu, T. T.; Li, L. Y.; Gao, P.; Li, L.; Cao, M. S. High-entropy electromagnetic functional materials: From electromagnetic genes to materials design. *Mater. Sci. Eng. R Rep.* 2025, *164*, **100982**.[DOI: 10.1016/j.mser.2025.100982]

[25] Qiu, Z.; Liu, X.; Yang, T.; et al., Synergistic enhancement of electromagnetic wave absorption and corrosion resistance properties of high entropy alloy through lattice distortion engineering. *Adv. Funct. Mater.* 2024, *34*, **2400220**.[DOI: 10.1002/adfm.202400220]

[26] Yu, L. Y.; Lan, D.; Guo, Z. Q.; et al., Multi-level hollow sphere rich in heterojunctions with dual function: Efficient microwave absorption and antiseptic. *J. Mater. Sci. Technol.* 2024, *189*, **155-65**.[DOI: 10.1016/j.jmst.2024.01.004]

[27] He, Y. F.; Su, Q.; Liu, D. D.; et al., Surface engineering strategy for MXene to tailor electromagnetic wave absorption performance. *Chem. Eng. J.* 2024, *491*, **152041**.[DOI: 10.1016/j.cej.2024.152041]

[28] Wu, G. R.; Han, Y.; Lan, D.; et al., Polyaniline decorative $MnCo_2O_{4.5}$ microspheres coupled with CoNi layered double hydroxides with remarkable electromagnetic wave absorption capacity. *Carbon* 2025, *244*, **120631**.[DOI: 10.1016/j.carbon.2025.120631]

[29] Han, Y.; Yang, Y.; Li, T.; et al., Hierarchical heterogeneous Co-based magnetic absorbers for superior broadband high-efficiency microwave absorption. *Adv. Funct. Mater.* 2026, *36*, **e25719**.[DOI: 10.1002/adfm.202525719]

[30] Zeng, X.; Cheng, X.; Yu, R.; Stucky, G. D. Electromagnetic microwave absorption theory and recent achievements in microwave absorbers. *Carbon* 2020, *168*, **606-23**.[DOI: 10.1016/j.carbon.2020.07.028]

[31] Peng, H.; Zhang, D.; Xie, Z.; et al., Recent advances in structural design of carbon/magnetic composites and their electromagnetic wave absorption applications. *Small* 2025, *21*, **2408570**.[DOI: 10.1002/smll.202408570]

[32] Fang, Y.; Wang, W.; Wang, S.; et al., A quantitative permittivity model for

designing electromagnetic wave absorption materials with conduction loss: A case study with microwave-reduced graphene oxide. *Chem. Eng. J.* 2022, *439*, **135672**.[DOI: 10.1016/j.cej.2022.135672]

[33] Wang, T.; Zhao, W.; Miao, Y.; et al., Enhancing defect-induced dipole polarization strategy of SiC@MoO_3 nanocomposite towards electromagnetic wave absorption. *Nano-Micro Lett.* 2024, *16*, **273**.[DOI: 10.1007/s40820-024-01478-2]

[34] Wang, T.; Chen, G.; Zhu, J.; et al., Deep understanding of impedance matching and quarter wavelength theory in electromagnetic wave absorption. *J. Colloid Interface Sci.* 2021, *595*, **1-5**.[DOI: 10.1016/j.jcis.2021.03.132]

[35] Sun, L. F.; Zhu, Q. Q.; Jia, Z. R.; et al., CrN attached multi-component carbon nanotube composites with superior electromagnetic wave absorption performance. *Carbon* 2023, *208*, **1-9**.[DOI: 10.1016/j.carbon.2023.03.021]

[36] Liu, Y.; Tian, C.; Wang, F.; et al., Dual-pathway optimization on microwave absorption characteristics of core-shell Fe_3O_4@C microcapsules: Composition regulation on magnetic core and MoS_2 nanosheets growth on carbon shell. *Chem. Eng. J.* 2023, *461*, **141867**.[DOI: 10.1016/j.cej.2023.141867]

[37] Gai, L.; Chen, Y.; Wang, Y.; et al., Engineering impedance-matched double-shells in hollow Co/carbon microspheres with gradient graphitization for high-efficiency electromagnetic wave absorption. *J. Adv. Ceram.* 2025, *14*, **9221212**.[DOI: 10.26599/JAC.2025.9221212]

[38] Cheng, J.; Jin, Y.; Zhao, J.; et al., From VIB- to VB-group transition metal disulfides: structure engineering modulation for superior electromagnetic wave absorption. *Nano-Micro Lett.* 2023, *16*, **29**.[DOI: 10.1007/s40820-023-01247-7]

[39] Wang, Y.; Han, X.; Xu, P.; et al., Synthesis of pomegranate-like Mo_2C@C nanospheres for highly efficient microwave absorption. *Chem. Eng. J.* 2019, *372*, **312-20**.[DOI: 10.1016/j.cej.2019.04.153]

[40] Zhang, S. T.; Wang, C. G.; Meng, X. W.; et al., Enhanced electromagnetic wave absorption of multicore Fe_4N@N-doped porous carbon core-shell microspheres through dielectric-magnetic coordination. *Carbon* 2025, *237*, **120176**.[DOI: 10.1016/j.carbon.2025.120176]

[41] Li, X.; Yin, S. F.; Cai, L.; et al., Sea-urchin-like $NiCo_2S_4$ modified MXene hybrids with enhanced microwave absorption performance. *Chem. Eng. J.* 2023, *454*, **140127**.[DOI: 10.1016/j.cej.2022.140127]

[42] Wang, P.; Gai, L.; Hu, B.; et al., Topological MOFs deformation for the direct

preparation of electromagnetic functionalized Ni/C aerogels with good hydrophobicity and thermal insulation. *Carbon* 2023, *212*, **118132**.[DOI: 10.1016/j.carbon.2023.118132]

[43] Liu, Z.; Wang, B.; Wei, S.; et al., Preparation and microwave-absorbing properties of FeCo alloys by condensation reflux method. *ACS Omega* 2024, *9*, **33692-701**.[DOI: 10.1021/acsomega.4c02330]

[44] Zhang, S.; Lan, D.; Zheng, J.; et al., Insights into polarization relaxation of electromagnetic wave absorption. *Cell Rep. Phys. Sci.* 2024, *5*, **102206**.[DOI: 10.1016/j.xcrp.2024.102206]

[45] Hu, B.; Chen, Y.; Chen, Y.; et al., Theoretical guidance for the rational design of FeCo foams toward efficient electromagnetic wave absorption in 2.0-8.0 GHz range. *Acta Phys.-Chim. Sin.* 2026, *42*, **100269**.[DOI: 10.1016/j.actphy.2026.100269]

[46] Han, G.; Li, M.; Liu, H.; et al., Short-range diffusion enables general synthesis of medium-entropy alloy aerogels. *Adv. Mater.* 2022, *34*, **2202943**.[DOI: 10.1002/adma.202202943]

[47] Zhang, X.; Qiao, J.; Jiang, Y.; et al., Carbon-based MOF derivatives: emerging efficient electromagnetic wave absorption agents. *Nano-Micro Lett.* 2021, *13*, **135**.[DOI: 10.1007/s40820-021-00658-8]

[48] Zhao, H.; Wang, F.; Cui, L.; et al., Composition optimization and microstructure design in MOFs-derived magnetic carbon-based microwave absorbers: a review. *Nano-Micro Lett.* 2021, *13*, **208**.[DOI: 10.1007/s40820-021-00734-z]

[49] Lin, J.; Liu, J.; Zhang, K.; et al., Ambient-pressure-dried aerogel amplifies interfacial polarization toward high-efficiency microwave absorption. *Adv. Funct. Mater.* 2026, *36*, **e20336**.[DOI: 10.1002/adfm.202520336]

[50] He, Z.; Huang, K.; Guo, C.; Jin, Z.; Hou, C. A Debye dispersion model of a two-layered material. *AIP Adv.* 2019, *9*, **045321**.[DOI: 10.1063/1.5085377]

[51] Djioko, J. P.; Atangana, J.; Edima, H. C. Spectral analysis of a dielectric material based on modified Debye model. *Arab. J. Sci. Eng.* 2023, *48*, **875-82**.[DOI: 10.1007/s13369-022-07159-9]

[52] Wang, Y.; Gai, L.; He, X.; et al., Sustainable upcycling of office waste paper into cobalt/carbon aerogels for highly efficient microwave absorption. *Electron* 2026, *4*, **e70029**.[DOI: 10.1002/elt2.70029]

[53] Li, N.; Wen, B.; Li, X.; et al., Phase structure-induced amplification of interfacial polarization loss for excellent electromagnetic wave absorption. *Chem. Eng. J.* 2024,

488, **150420**.[DOI: 10.1016/j.cej.2024.150420]

[54] Wang, F.; Liu, Y.; Feng, R.; et al., A “win-win” strategy to modify Co/C foam with carbon microspheres for enhanced dielectric loss and microwave absorption characteristics. *Small* 2023, *19*, **2303597**.[DOI: 10.1002/smll.202303597]

[55] Wang, P.; Fan, D.; Gai, L.; et al., Synthesis of graphene oxide-mediated high-porosity Ni/C aerogels through topological MOF deformation for enhanced electromagnetic absorption and thermal management. *J. Mater. Chem. A* 2024, *12*, **8571-82**.[DOI: 10.1039/D4TA00125G]

[56] Liu, Y.; Wang, F.; Wang, Y.; et al., A combined engineering of hollow and core-shell structures for C@MoS_2 microcapsules toward high-efficiency electromagnetic absorption. *Compos. Part B Eng.* 2024, *273*, **111244**.[DOI: 10.1016/j.compositesb.2024.111244]

[57] Qi, J.; Liang, C.; Ruan, K.; et al., Cactus-like architecture for synergistic microwave absorption and thermal management. *Natl. Sci. Rev.* 2025, *12*, **nwaf394**.[DOI: 10.1093/nsr/nwaf394]

[58] Qiao, L.; Wang, T.; Mei, Z. L.; et al., Analyzing bandwidth on the microwave absorber by the interface reflection model. *Chin. Phys. Lett.* 2016, *33*, **027502**.[DOI: 10.1088/0256-307X/33/2/027502]

[59] Sun, X.; Li, Y.; Huang, Y.; et al., Achieving super broadband electromagnetic absorption by optimizing impedance match of rGO sponge metamaterials. *Adv. Funct. Mater.* 2022, *32*, **2107508**.[DOI: 10.1002/adfm.202107508]

[60] Chen, Y.; Gai, L.; Hu, B.; et al., Directional three-dimensional macroporous carbon foams decorated with WC_{1-x} nanoparticles derived from salting-out protein assemblies for highly effective electromagnetic absorption. *Nano-Micro Lett.* 2025, *18*, **71**.[DOI: 10.1007/s40820-025-01920-z]

[61] Ding, H.; Li, Y.; Wang, Y.; et al., Entropy-mediated lattice distortion for tailored dielectric polarization to improve L-band electromagnetic wave absorption. *Nano-Micro Lett.* 2026, *18*, **358**.[DOI: 10.1007/s40820-026-02203-x]